IEEE Access
Multidisciplinary | Rapid Review | Open Access Journal

Received January 15, 2022, accepted January 26, 2022, date of publication February 28, 2022, date of current version March 14, 2022.

Digital Object Identifier 10.1109/ACCESS.2022.3155158

Multimodal Optimization Algorithm for Torque Ripple Reduction in Synchronous Reluctance Motors

MOEIN FARHADIAN[1], MEHDI MOALLEM[1], (Senior Member, IEEE), AND BABAK FAHIMI[2], (Fellow, IEEE)

[1]Department of Electrical and Computer Engineering, Isfahan University of Technology, Isfahan 84156, Iran
[2]Department of Electrical and Computer Engineering, University of Texas at Dallas, Richardson, TX 75080, USA

Corresponding author: Babak Fahimi (fahimi@utdallas.edu)

ABSTRACT An accurate analytical model is adopted to estimate the torque ripple of a synchronous reluctance motor (SynRM). Desired behavior of the torque ripple functionin this motor is obtained by changing the angles of one and two flux barriers per pole (FBs) in the rotor. The torque ripple function of the SynRM serves as the multiple and close local optima. By identifying the behavior of this function, a comprehensive learning particle swarm optimization (CLPSO) algorithm (typically applied in solving multimodal functions), is adopted to reduce the torque ripple. The results indicate that compared to PSO (i.e. global optimization algorithms) the CLPSO algorithm is more efficient in torque ripple reduction and finding more local optima. Among the available optimal solutions with four FBs per pole, a sample is selected for motor construction. Finite element analysis and laboratory tests are performed to validate the results.

INDEX TERMS Synchronous reluctance machine, multimodal optimization, torque ripple.

I. INTRODUCTION

To design a synchronous reluctance motor (SynRM), the rotor configuration, method of analyzing the motor performance, and optimization algorithm constitute the fundamental components. The configuration of a SynRM rotor for obtaining high reluctance difference is subject to placing multiple conductive and insulating magnetic layers. In transversally laminated rotors, a popular theme of study in the literature (due to its easy manufacturing process), is to have magnetic insulators implemented by air voids, also referred to as flux barriers (FB)s in the rotor's magnetic sheets.

The FBs' shape can take straight lines (rectangular, trapezoidal [1]), curves (circular [2], [3], crescent [4]–[6], hyperbolic[7], etc.), or a combination of straight lines and curves [8]. The main objective of these various shapes is to optimally chanel the flux lines within a solid rotor. The shape of FBs can be expressed by analytically [9]. The findings of most studies reveal the superiority of the fluid shaped, the Zhukovski shaped, and field path design geometry, for FBs when compared to other shapes [10], [11].

The associate editor coordinating the review of this manuscript and approving it for publication was Paolo Giangrande.

The methods applied in analyzing the performance of electric machines are grouped into two general categories namely, numerical and analytical. The finite element analysis (FEA) with high precision is widely applied in design of SynRM. The main problem in applying FEA to design of SynRM is attributed to its prolonged computational time in view ofthe large number of design variables. Reducing torque calculation points by randomly selecting them within the optimization iterations [12], surrogate models like Kriging [13], computationally efficient electromagnetic FEA [14], and combining FEA with analytical methods [1] are among the measures that has been taken in reducing the computational cost.

As to the analytical methods, they are faster than FEA, with a high possibility to evaluate more cases in achieving the optimal solution. Obtaining an analytical model for SynRM usually involves simplifying assumptions that reduce its accuracy. The initial analytical models [15], regardless of the effect of the stator slots, merely estimate the radial component of the air gap magnetic field. Consequently, stator slotting effect in radial magnetic field modeling was added using permeance functions [16]. In addition to the radial component, the tangential part of the magnetic field is estimated

This work is licensed under a Creative Commons Attribution 4.0 License. For more information, see https://creativecommons.org/licenses/by/4.0/

by combining the magnetic equivalent circuit (MEC) and conformal mapping (CM) methods [17].

Maximizing average torque and minimizing torque ripple are the two main objectives in SynRM optimization. In multi-objective optimization, these two are considered simultaneously [18]. In some studies, these two are optimized independently [1], and it is reported that these two objectives are not conflicting [1]. There exist many locally optimal solutions using which the problem of SynRM optimization is characterized. In [18] and in order to find more optimal solutions, optimization is done in two stages. First a more extensive range is considered for the variables, and several iterations are performed towards finding the global optima. This is followed by a zoomed local search around the potential solutions obtained in the first stage with a smaller range for the variables.

In this paper, the average torque and torque ripple objectives are optimized independently. The analytical model is applied to optimize the SynRM torque ripple. Instead of running repeated optimizations to assure the optimality of the solutions, the behavior of the torque ripple function for one or two FBs is determined using parametric analysis (incorporating an analytical model that allows rapid evaluation of motor performance). At this juncture a comprehensive learning particle swarm optimization (CLPSO) algorithm is applied, and its performance is compared to that of the PSO algorithm. After performing torque ripple optimization, the sample of optimal rotors in terms of torque ripple is selected for average torque optimization, and the best candidate is designated for construction and laboratory examination.

II. ANALYTICAL COMPUTATION OF TORQUE RIPPLE

The analytical model is based on combination of the MEC and CM methods, which allows for much faster calculation of torque ripple when compared to FEA. In this section, the analytical modeling of SynRM is briefly described; More details can be found in [17].

In the first step, by disregarding the rotor FBs, the components of the air gap magnetic field (formed from the stator winding) are calculated using CM. Following this, the potential magnetic drop due to the rotor FBs is calculated through linear MEC and the radial component of the magnetic field obtained in the first step. Consequently the possible reduction, due to the rotor, is applied through virtual currents in the CM method. The air gap magnetic field is equal to the resultant of the stator winding magnetic field and the virtual magnetic field of the FBs. This modeling method makes it possible to obtain radial and tangential components of the magnetic field by considering the rotor FBs effect.

The stator of an induction motor is selected to design the SynRM. One magnetic pole along with a rotor having two FBs per pole is shown in Fig. 1, and the stator parameters are tabulated in Table 1.

The rotor pole with the two FBs is shown in Fig. 2. Symbols $\Delta\alpha_1$ and $\Delta\alpha_2$ are the angles of the first and second FBs, and W_1 and W_2 are the thicknesses of the first and second

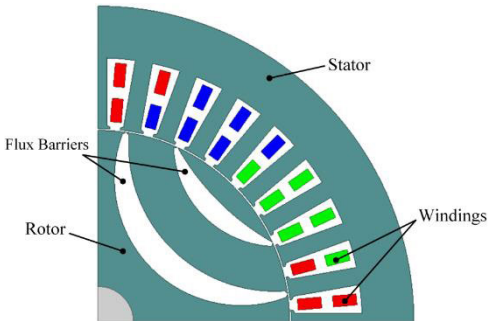

FIGURE 1. Cross section of one pole from the motor under study.

TABLE 1. Geometric parameters of the motor.

Parameter	Unit	Value
Stack length	[mm]	40
Stator outer diameter	[mm]	152
Stator inner diameter	[mm]	93
Shaft diameter	[mm]	25
Air gap thickness	[mm]	0.4
Slot opening	[mm]	2.53
Slot numbers	-	36
Pole pairs	-	2
Turns per slot	-	80

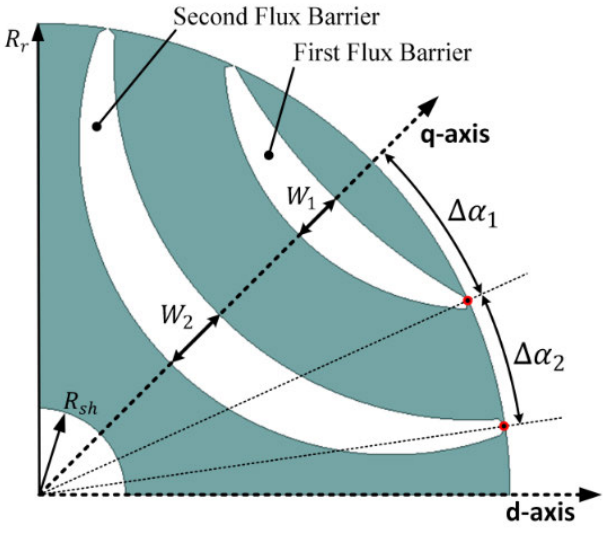

FIGURE 2. Definition of parameters for flux barriers.

FBs along the q-axis, respectively. Radial air gap magnetic fields formed by stator windings, FBs, and their sum obtained through the analytical model are shown in Fig. 3. The FBs form a virtual magnetic field opposite to the direction of the magnetic field, formed by the stator winding. Due to the two-layer FBs, two steps drop is created in the air gap magnetic field. The total magnetic field of the air gap equals the resultant of the field of stator winding and the virtual fields of the FBs.

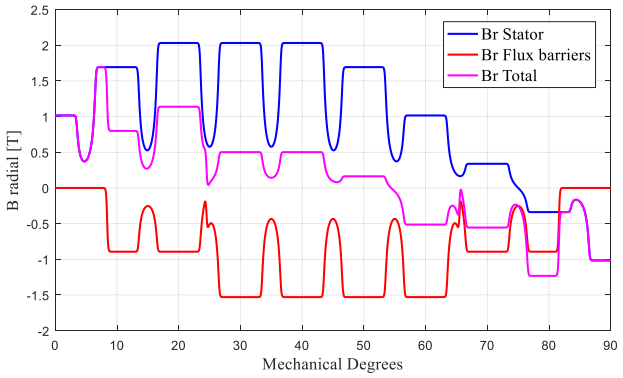

FIGURE 3. Radial components of the air gap magnetic field due to the stator, FBs, and their sum.

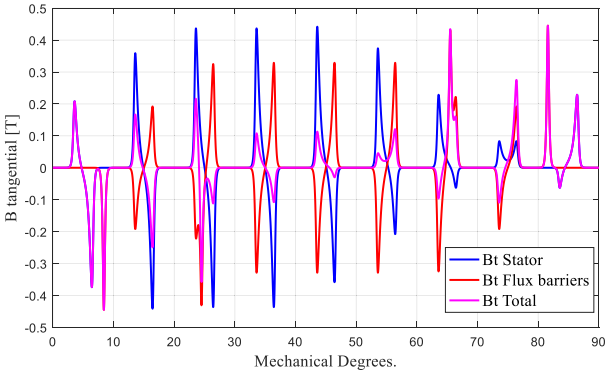

FIGURE 4. Tangential components of the air gap magnetic field due to the stator, FBs, and their sum.

The tangential magnetic fields of the stator winding, the FBs, and their sum are shown in Fig. 4. Similar to the previous case, the tangential magnetic field generated by the FBs is in the opposite direction of the stator field, leading to drops in the tangential component in the area between the FBs. Due to the rotation of the flux lines at the location of the end angles of the FBs, drastic changes in the tangential component of the air gap magnetic field are observed.

The radial and tangential components of the total air gap magnetic field, in comparison with the FEA results, are shown in Figs. 5 and 6 respectively. As observed, there exists a good agreement between the results obtained by the analytical method and the FEA.

Variations of the motor torque(with the aforementioned three steps in the stator slot) and for the rotor of Fig. 2 in which only the second FB angle is reduced by one degree is shown in Fig. 7.

In both cases, the results of the analytical model are in good agreement with that of the FEA. For angles $\Delta\alpha_1 = 20.5°$ and $\Delta\alpha_2 = 16.1°$, the torque ripple is 30.5%, and for angles $\Delta\alpha_1 = 20.5°$ and $\Delta\alpha_2 = 15.1°$, the torque ripple increases to 62.1%. As observed by changing one degree of the second FB arc, the torque ripple almost doubles, indicating the high sensitivity of the torque ripple to the end angles of the

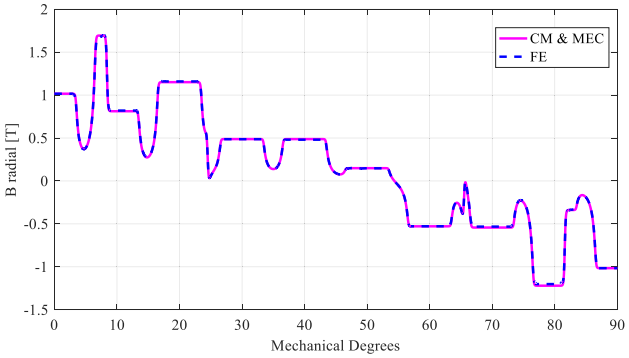

FIGURE 5. Radial air gap magnetic field computed through FEA and analytically.

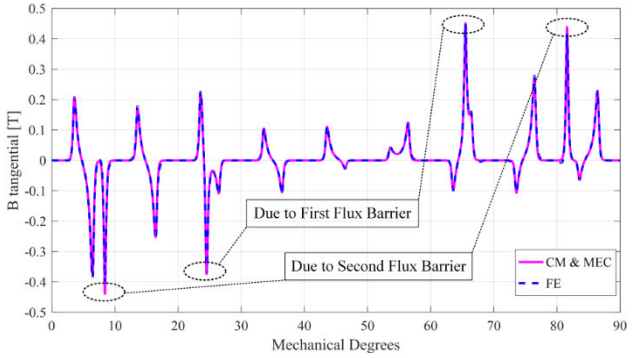

FIGURE 6. Tangential air gap magnetic field computed through FEA and analytically.

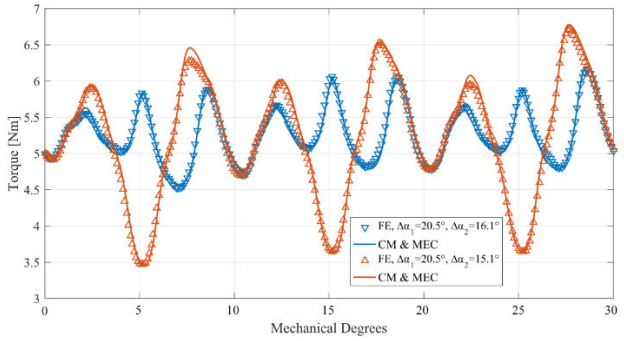

FIGURE 7. Electromagnetic Torque computed through FEA and analytical model.

FBs; consequently, torque ripple optimization is necessary to determine the optimal angles.

III. PARAMETRIC ANALYSIS

A. ONE FB PER POLE

To assess the impact of the FB angle on torque ripple, in the rotor with one FB, the FB angle is changed from 15° to 45° with a step of 0.01°. The time required to compute the objective function consisting of 30 points of the torque curve (using the analytical model in three steps of the stator slot) sums to about 3.5 seconds using a Core i5-2.6GHz processor.

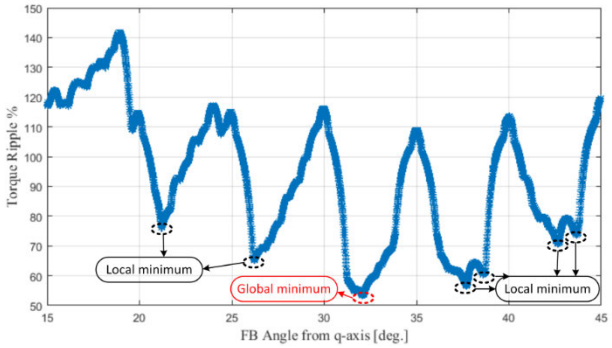

FIGURE 8. Torque ripple results for changing the angle of a FB.

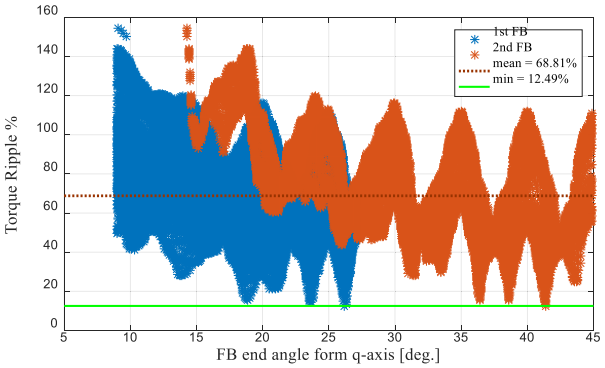

FIGURE 9. Torque ripple results for changing the FBs angle.

This suggests that the time required to calculate all cases (e.g. 3000 times) is about 3 hours. Although it is recommended to avoid choosing a FB per pole for the SynRM due to its inferior performance [19], practical information is found in Fig. 8, where the torque ripple function has many local optima, with short distances between some local optima.

B. TWO FB PER POLE

To reduce the simulation time for two FBs per pole, a parametric analysis is run by reducing the step to 0.1° for the angle of each FB. The angle of the first FB is changed between 0.2 and 0.6 per unit (relative to the half pole pitch), and the angle of the second FB is changed between 0.1 and 0.5 per unit, requiring over 30,000 objective function calls. Due to the 2D space of the parameters, by selecting the 0.01° step, the number of times for which the objective function is called will be 100 times greater than the case with 0.1° step.

The torque ripple function is shown in 2D and 3D illustrations in Figs. 9 and 10, respectively, Similar to the rotor with one FB, the torque ripple function has multiple local minima; while, the global minimum value is drastically reduced compared to the rotor with one FB. As observed in Fig. 9, the difference between some local minima and a global minimum is negligible; therefore, with different combinations of FB angles, torque ripple can be reduced to the vicinity of the global minimum.

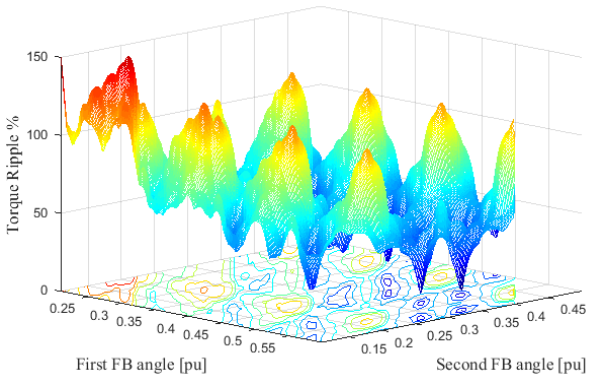

FIGURE 10. Torque ripple function for changing two FBs angle.

IV. TORQUE RIPPLE OPTIMIZATION

In the following, PSO and CLPSO algorithms are used for torque ripple optimization, and their performances are compared. First, these two algorithms are briefly introduced.

A. PSO ALGORITHM

In PSO algorithm, every particle is an answer to the problem, which moves in the search space based on the best individual flight experience and the best group flight experience. Each particle i contains the position (X_i^d), velocity (V_i^d), and its best individual position ($pbest_i^d$) data. Index d is the particle dimension. The particles are randomly scattered in the search space with zero velocity. Each particle moves according to the laws of velocity (1) and position (2) [20]:

$$V_i^d \leftarrow w.V_i^d + c_1.rand1_i^d.\left(pbest_i^d - X_i^d\right) + c_2.rand2_i^d.(gbest_i^d - X_i^d) \quad (1)$$

$$X_i^d \leftarrow X_i^d + V_i^d \quad (2)$$

where w, c_1, and c_2 are the parameters of the algorithm, named as the weight of inertia, the acceleration coefficient of the individual, and social components, respectively. The weight of inertia has a diverse contribution, and the acceleration coefficients seek to converge the algorithm. Symbols $rand1_i^d$ and $rand2_i^d$ are the two random numbers between zero and one that determine the probable nature of the algorithm. Symbol $pbest_i^d$ is the best position of the i^{th} particle, and $gbest^d$ is the best position ever.

B. CLPSO ALGORITHM

All-particle memory information is applied to the CLPSO algorithm to update the new particle position. This feature allows for the dispersal of particles and prevents rapid convergence. The velocity equations in CLPSO are modified as (3) [21].

$$V_i^d \leftarrow w * V_i^d + c * rand_i^d * (pbest_{fi(d)}^d - X_i^d) \quad (3)$$

where $f_i = [f_i(1), f_i(2), \ldots, f_i(D)]$ determines which particles' *pbest* positions should be applied in the i^{th} particle. For each particle dimension, a random number is generated;

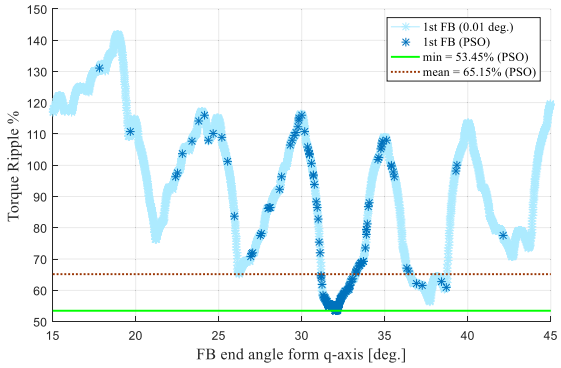

FIGURE 11. PSO's results on torque ripple optimization with one FB.

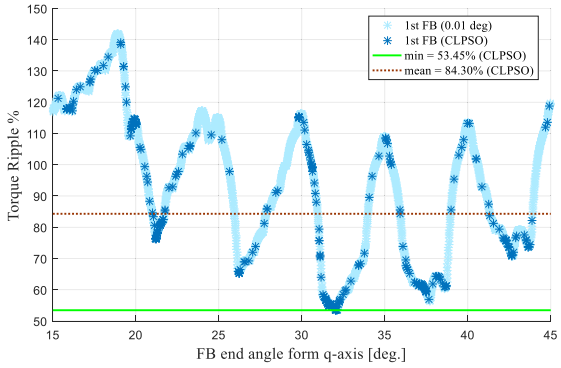

FIGURE 12. CLPSO's results on torque ripple optimization with one FB.

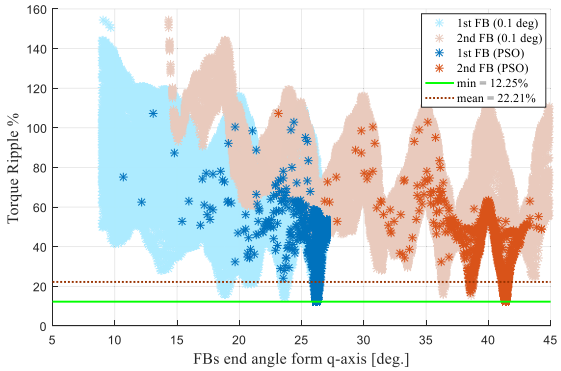

FIGURE 13. PSO's results on torque ripple optimization with two FBs.

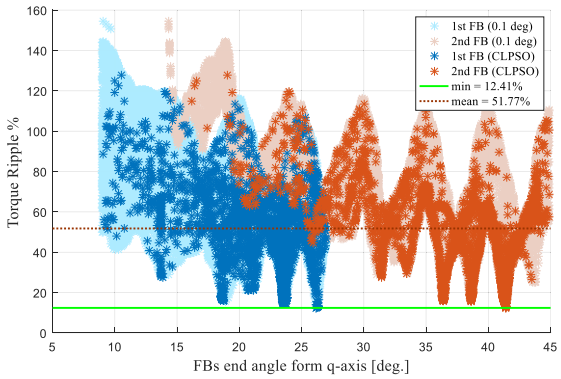

FIGURE 14. CLPSO's results on torque ripple optimization with two FBs.

if less than P_c, the *pbest* of the particle itself is selected for the proper dimension, otherwise, the *pbest* of other particles is selected based on the tournament selection. The differences between PSO and CLPSO algorithms are [21]:

1. Instead of applying a particle's *pbest* and *gbest* as the exemplars, all particles' *pbest* can potentially be applied as the exemplars to guide a particle's flying direction.
2. Instead of applying all the dimensions of an exemplar, each particle dimension can take its new position from the dimension of different particles.
3. Instead of learning from the two *pbest* and *gbest* exemplars in each generation, each particle can use only one exemplar in a limited number of repetitions for learning.

The performance of CLPSO algorithm with eight different types of PSO algorithms in optimization for different objective functions is assessed in [21]; in most multimodal cases, CLPSO outperforms PSO variants.

C. ONE AND TWO FB PER POLE

The objective function is to minimize torque ripple. The optimization constraints for FBs are similar to that of the parametric analysis mode. Like the previous case, 30 points of the torque curve in three stator slot steps are considered to evaluate the torque ripple. The initial population is generated randomly. The number of function evaluations for the rotor with one and two FBs per pole is selected to be 300 and 3000 times, respectively. This is almost ten times less than the number of calls in the parametric analysis with fixed-step. For better comparison, the parameters of both algorithms are selected to be the same. The results of torque ripple optimization with a FB by PSO and CLPSO algorithms in the background of the parametric analysis are shown in Figs. 11 and 12, respectively.

The optimization results indicate that in PSO algorithm most of the particles are gathered around the global minimum, while in CLPSO algorithm, the same particles are subject to higher dispersion, thus, they can be found at all local minima's. Both algorithms with similar accuracy have reached the global minimum solution, at 53.45%, obtained through the parametric analysis with a 0.01° step. The average of the solutions in the PSO is 19.15% less than that of the CLPSO.

The results of torque ripple optimization with two FBs per pole obtained through PSO and CLPSO algorithms are shown in Figs. 13 and 14, respectively.

By comparing the results observed in Figs. 13 and 14, both algorithms have reached the global minimum obtained through the parametric analysis (with slightly higher accuracy). The optimization results obtained through PSO algorithm have one local minimum for the first FB and two local minima for the second FB, which have a ripple value of less than 20%; while the same through CLPSO algorithm

TABLE 2. Optimization constraints.

Parameter	Lower limit	Upper limit	Unit
$\Delta\alpha_1$	0.2	0.6	p.u.
$\Delta\alpha_i$ (i =2,…, N_b)	0.1	0.5	p.u.
$\sum_i^{N_b} \alpha_i < 1 \quad (i = 1,..., N_b)$			p.u.

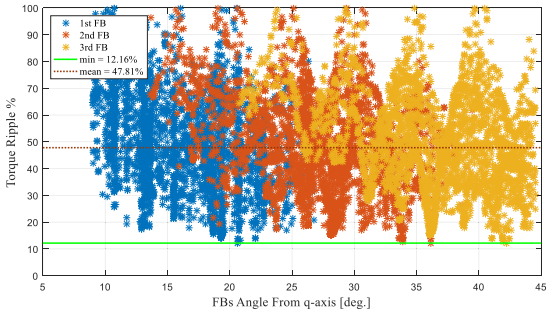

FIGURE 15. CLPSO's results on torque ripple optimization with three FBs.

for both FBs reveals three local minima of less than 20%. Particle diversity in the CLPSO algorithm is higher than that of the PSO algorithm, with more local optimal solutions. The high convergence of the PSO algorithm necessitates repetitive executions to find more local optima.

D. THREE AND FOUR FB PER POLE

As the number of FBs increases, sensitivity analysis, even with a 0.1° step for the angle of each FB, leads to an intensive computational time. Though the analytical model is faster than FEA, here, to limit the execution time to an acceptable level, optimization algorithms must be applied. Because in rotors with one and two FBs per pole, CLPSO outperforms the PSO algorithm, it is applied to optimize the rotors with three and four FBs per pole. Theoretically, there is no limit to the number of FBs, but in small motors, to reduce the shear level and maintain the mechanical strength of the rotor, the number of FBs usually does not exceed four for each pole.

The constraints of parameters are tabulated in Table 2. The first FB can be changed between 0.2 and 0.6 per unit, and the rest can be changed from 0.1 to 0.5 per unit. During initialization, the random production of all the particles continues until satisfying the constraints. During iterations, to keep the particles in the feasible space, the objective function is computed for the particles, and the *pbest* and *gbest* values are updated only if the particle is in the feasible space. Because all particles are in the feasible space, the particle eventually returns to the feasible region.

The optimization results for the rotor with three and four FBs per pole are shown in Figs. 15 and 16, respectively. As the FBs number increases, the global optimum torque ripple, and the average of the total solutions decreases.

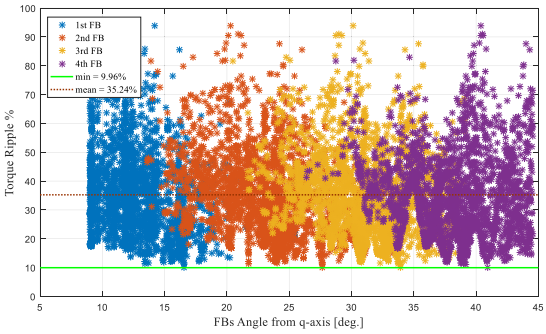

FIGURE 16. CLPSO's results on torque ripple optimization with four FBs.

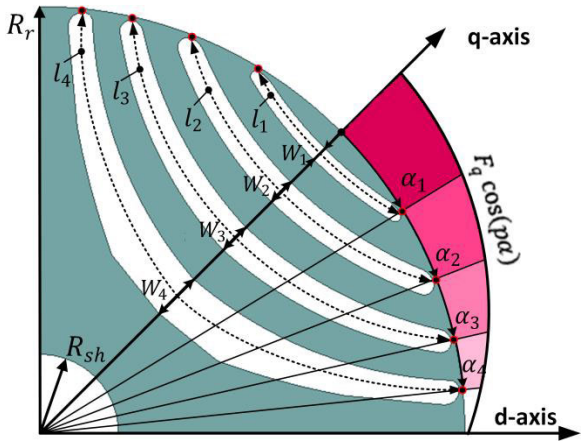

FIGURE 17. Definition of rotor parameters and *q*-axis MMF distribution.

Because the optimal rotors with four ripple FBs per pole are of less torque ripple compared to others, few samples are selected, based on suitability for manufacturing, to determine the FBs' thickness and further assessments.

V. AVERAGE TORQUE OPTIMIZATION

The FBs' thickness is an effective parameter in the average torque with a slight impact on the torque ripple; therefore, by changing this thickness, the optimal average torque value can be obtained. In assessing the FBs' thickness effect on average torque, the application of a parameter named insulation ratio has been common [9], [22], [23]. The insulation ratio (k_{ins}) is defined as the total FBs' thickness along the q-axis to the rotor thickness ratio obtained through (4) [24]:

$$k_{ins} = \frac{\sum_i^{N_b} W_i}{R_r - R_{sh}} \tag{4}$$

where, W_i is the thickness of the i^{th} FB along the q-axis, N_b is the number of the FBs, R_r is the rotor radius, and R_{sh} is the shaft radius. Selecting any value for k_{ins} gives the total thickness of the FBs, but does not determine the thickness of each FB.

The thickness of each FB should be adjusted to reduce the q-axis flux at its highest. A pole of the synchronous reluctance rotor and the principal component of the q-axis magnetomotive force (MMF) distribution is shown in Fig. 17. The method

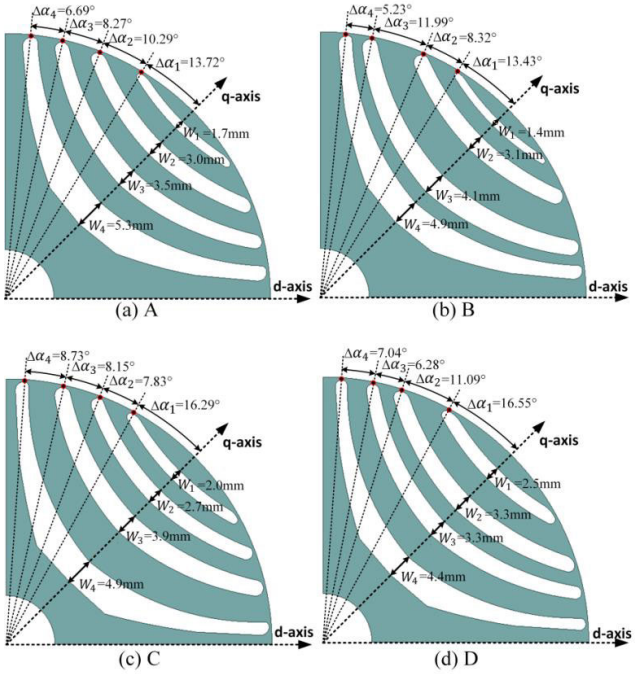

FIGURE 18. Selected optimal rotors a(A), b(B), c(C), and d(D).

applied below is based on the results given in [22]. It has been proven that if (5) is established between the thickness of the FBs, the inductance (flux) of the q-axis will be minimal.

$$\frac{W_i}{W_j} = \frac{\Delta F_{q,i}}{\Delta F_{q,j}} \sqrt{\frac{l_i}{l_j}} \approx \frac{\Delta F_{q,i}}{\Delta F_{q,j}} \sqrt{\frac{\alpha_i}{\alpha_j}} \tag{5}$$

where, l_i is the length of the i^{th} FB. Symbol $\Delta F_{q,i}$ denotes the difference in the average per-uint of the MMF ($F_{avg,i}$) in the i^{th} FB, calculated through (6).

$$\begin{cases} F_{avg,i} = \dfrac{1}{\alpha_i - \alpha_{i-1}} \displaystyle\int_{\alpha_{i-1}}^{\alpha_i} F_q \cos(p\alpha)\, d\alpha, & 1 \le i \le N_b \\ \Delta F_{q,i} = F_{avg,i} - F_{avg,i+1} & 1 \le i \le N_b - 1 \\ \Delta F_{q,N_b} = F_{avg,N_b} & i = N_b \end{cases} \tag{6}$$

By determining the insulation ratio and the FBs' width ratio, it is easy to obtain each FB's width. By selecting the optimal points for the FB angles, location of FBs are restricted.

Four of the optimal rotor solutions in torque ripple, with four FBs per pole, named A, B, C, and D, are selected to determine FBs' width. The rotors with an insulation ratio of 0.4 are shown in Fig. 18. The flux line pattern is selected for FBs' shape to achieve the maximum torque.

The results of changing the insulation ratio on the average torque and peak-to-peak torque ripple of the motors are shown in Figs. 19 and 20, respectively. The motors' torque is obtained at the current angle that produces the maximum torque. The FEA (using M400 magnetization curve) is applied for evaluation.

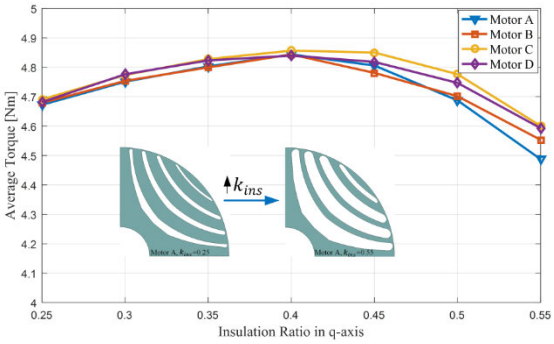

FIGURE 19. Effect of increasing insulation ratio on average torque.

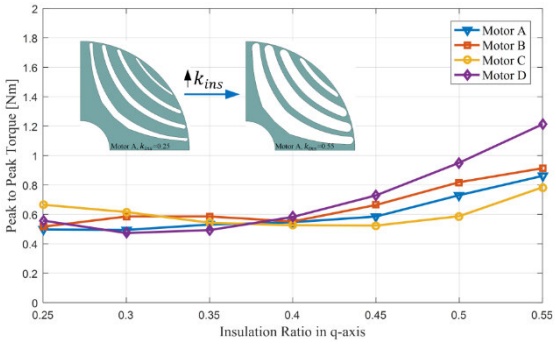

FIGURE 20. Effect of increasing insulation ratio on torque ripple.

TABLE 3. Torque ripple computation using analytical and FEA methods.

Rotor type	$\Delta\alpha_1$	$\Delta\alpha_2$	$\Delta\alpha_3$	$\Delta\alpha_4$	Ripple % Analytical	Ripple % FEA	Error %
A	13.7	10.3	8.27	6.7	11.64	11.54	0.10
B	13.4	8.32	12.0	5.2	12.11	11.28	0.83
C	16.3	7.83	8.15	8.7	12.14	10.83	1.31
D	16.5	11.1	6.28	7.0	11.94	12.05	0.11

As shown in Fig. 19 the behavior of the four motors is similar. An increase in the insulation ratio increases the the average torque, because as the FBs' thickness increases, the inductance of the q-axis decreases, while there is still enough iron to cross the d-axis flux. When the insulation ratio reaches 0.4, the maximum average torque is obtained for all four motors. By increasing the insulation ratio from 0.4, the effect of iron saturation reduces the d-axis' flux and decreases the average torque.

Between the 0.25 to 0.4 insulation ratios, the peak-to-peak torque of the four motors is almost constant. Furthermore, increase in insulation ratio increases the peak-to-peak torque due to the nonlinear effects of the saturation curve. The comparison of torque ripple calculation with the analytical model and FEA for optimal motors with insulation ratio of 0.4 is listed in Table 3. There exists a good agreement between the results of the two methods, and the maximum error of torque ripple is 1.31%. The Motor-C is selected for construction

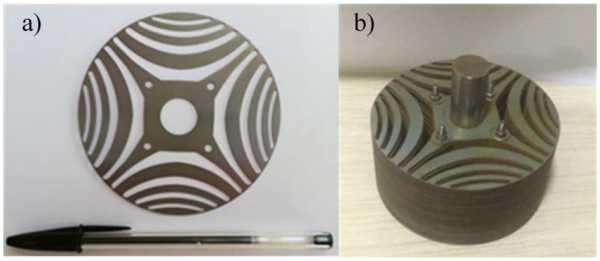

FIGURE 21. (a) Single lamination of the rotor. (b) Rotor stack with embedded shaft.

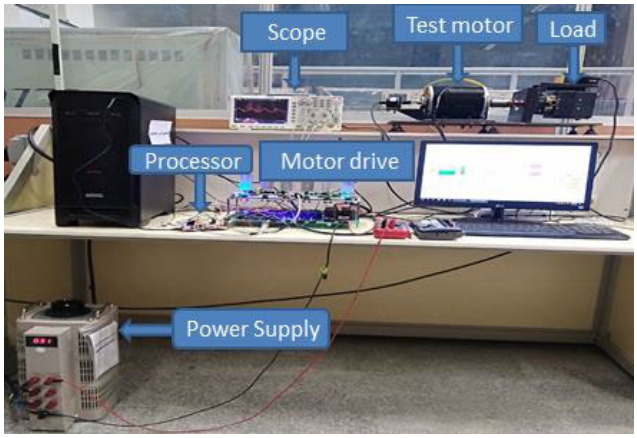

FIGURE 22. Test bench.

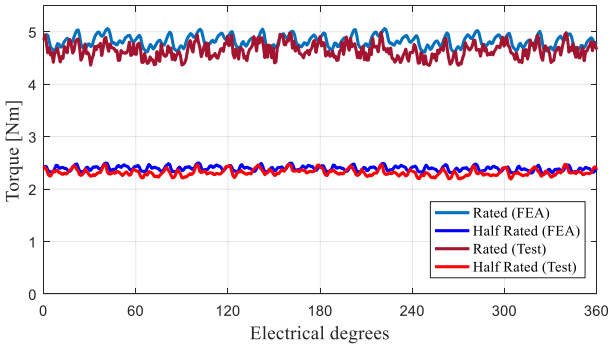

FIGURE 23. Torque waveform in rated and half rated values.

TABLE 4. Performance of the motor under rated condition.

Parameter	Unit	FEA	Test
Speed	rpm	1500	1499
Torque	N.m	4.77	4.79
Output Power	W	750	752
Current	A	2.25	2.26
Core loss	W	28.3	34.2
Ohmic loss	W	83.5	84.3
Windage loss	W	7.0	7.0
Total loss	W	118.8	125.4
Efficiency	%	86.32	85.71

because of its superiority in terms of average torque and torque ripple.

VI. EXPERIMENTAL RESULTS

The M400-50A magnetic sheet is used in manufacturing of the rotor. The laminations are cut by the electric discharge machining method. In Fig. 21 (a), a sample of the rotor lamination, and (b) the rotor stack without any skew, with a dummy shaft are illustrated. The rotor ribs are tangential only, with 0.4 mm thickness. The test bench is shown in Fig. 22. A DSP board controls the motor, and current vector control is applied to drive it. The maximum torque per ampere (MTPA) control strategy is applied at each torque level.

A. MEASURED AND SIMULATED TORQUE

The test motor is rotated at a low speed (10 rpm) to confirm the motor torque ripple behavior. Two current levels of 2.3A at 60° and 1.5A at 50° are considered for comparison. For each combination of d and q-axis currents in a complete rotor rotation, the torque waveform is recorded with a torque transducer. The measurement and the simulation torque at two levels of rated and half-rated values are shown in Fig. 23. The measured values of torque are in good agreement with the simulation values. As expected, there exists a direct relation between the torque ripple and current.

B. EFFICIENCY

Full-load and no-load tests are run on the prototype motor. The results of FEA simulation and laboratory tests are tabulated in Table 4. There exists a good agreement between the simulation and laboratory results. Motor efficiency is 85.71%, which reaches the IE4 class.

VII. CONCLUSION

The performance of PSO and CLPSO algorithms, appropriate for solving unimodal and multimodal problems, are compared for the optimization of the torque ripple of a SynRM using an analytical model to determine which algorithm is more appropriate for machine optimization. The results indicate that both algorithms yield the same global optimal solution, while the CLPSO algorithm finds more local optima than the PSO algorithm.

The analytical model offers a good accuracy in the linear region of the magnetization curve, however, its accuracy declines as magnetic saturation increases. The behavior of torque ripple function for SynRM with one and two FBs is determined through the analytical model. By changing the angle of the FBs, the torque ripple function reveals many local optima, the value of which is not very different from the global optimal. The accuracy of the optimal solutions is evident through FEA, and one of the optimal rotors is selected for construction. The laboratory tests and FEA show the computational efficiency of the optimization method.

In most electric machine design problems, the shape of the objective function is unknown, consequently, it is recommended to apply an optimization algorithm capable of solving multimodal problems. Because algorithms applied in solving multimodal problems can solve unimodal problems

as well, by applying multimodal optimization algorithms, important information on some local optima becomes is lost.

REFERENCES

[1] R.-R. Moghaddam and F. Gyllensten, "Novel high-performance SynRM design method: An easy approach for a complicated rotor topology," *IEEE Trans. Ind. Electron.*, vol. 61, no. 9, pp. 5058–5065, Sep. 2014, doi: 10.1109/TIE.2013.2271601.

[2] X. B. Bomela and M. J. Kamper, "Effect of machine design on performance of reluctance synchronous machine," in *Proc. Conf. Rec. IEEE Ind. Appl. Conf., 35th IAS Annu. Meeting World Conf. Ind. Appl. Elect. Energy*, vol. 1, Oct. 2000, pp. 515–522.

[3] M. J. Kamper, F. S. V. D. Merwe, and S. Williamson, "Direct finite element design optimisation of the cageless reluctance synchronous machine," *IEEE Trans. Energy Convers.*, vol. 11, no. 3, pp. 547–555, Sep. 1996, doi: 10.1109/60.537006.

[4] M. H. A. Prins, C. W. Vorster, and M. J. Kamper, "Reluctance synchronous and field intensified-PM motors for variable-gear electric vehicle drives," in *Proc. IEEE Energy Convers. Congr. Expo.*, Sep. 2013, pp. 657–664.

[5] A. Tessarolo, "Modeling and analysis of synchronous reluctance machines with circular flux barriers through conformal mapping," *IEEE Trans. Magn.*, vol. 51, no. 4, pp. 1–11, Apr. 2015, doi: 10.1109/TMAG.2014.2363434.

[6] S. Stipetic, D. Zarko, and N. Cavar, "Design methodology for series of IE4/IE5 synchronous reluctance motors based on radial scaling," in *Proc. 13th Int. Conf. Electr. Mach. (ICEM)*, Sep. 2018, pp. 146–151, doi: 10.1109/ICELMACH.2018.8507100.

[7] A. Kersten, Y. Liu, D. Pehrman, and T. Thiringer, "Rotor design of line-start synchronous reluctance machine with round bars," *IEEE Trans. Ind. Appl.*, vol. 55, no. 4, pp. 3685–3696, Jul. 2019, doi: 10.1109/TIA.2019.2914010.

[8] E. Howard, M. J. Kamper, and S. Gerber, "Asymmetric flux barrier and skew design optimization of reluctance synchronous machines," *IEEE Trans. Ind. Appl.*, vol. 51, no. 5, pp. 3751–3760, Sep./Oct. 2015.

[9] R. R. Moghaddam, "Synchronous reluctance machine (SynRM) in variable speed drives (VSD) applications," Ph.D. dissertation, KTH School Elect. Eng., KTH Roy. Inst. Technol., Stockholm, Sweden, 2011.

[10] M. Gamba, G. Pellegrino, and F. Cupertino, "Optimal number of rotor parameters for the automatic design of synchronous reluctance machines," in *Proc. Int. Conf. Electr. Mach. (ICEM)*, Sep. 2014, pp. 1334–1340, doi: 10.1109/ICELMACH.2014.6960355.

[11] S. Yammine, C. Henaux, M. Fadel, S. Desharnais, and L. Calegari, "Synchronous reluctance machine flux barrier design based on the flux line patterns in a solid rotor," in *Proc. Int. Conf. Electr. Mach. (ICEM)*, Sep. 2014, pp. 297–302, doi: 10.1109/ICELMACH.2014.6960196.

[12] G. Pellegrino, F. Cupertino, and C. Gerada, "Automatic design of synchronous reluctance motors focusing on barrier shape optimization," *IEEE Trans. Ind. Appl.*, vol. 51, no. 2, pp. 1465–1474, Apr. 2015.

[13] S. Guenther and W. Hofmann, "Multi-objective tradeoffs in the design optimization of synchronous reluctance machines for electric vehicle application," in *Proc. IEEE Int. Electr. Mach. Drives Conf. (IEMDC)*, May 2015, pp. 1715–1721, doi: 10.1109/IEMDC.2015.7409295.

[14] Y. Wang, D. M. Ionel, M. Jiang, and S. J. Stretz, "Establishing the relative merits of synchronous reluctance and PM-assisted technology through systematic design optimization," *IEEE Trans. Ind. Appl.*, vol. 52, no. 4, pp. 2971–2978, Jul./Aug. 2016, doi: 10.1109/TIA.2016.2544831.

[15] N. Bianchi, S. Bolognani, D. Bon, and M. D. Pré, "Torque harmonic compensation in a synchronous reluctance motor," *IEEE Trans. Energy Convers.*, vol. 23, no. 2, pp. 466–473, Jun. 2008.

[16] A. Tessarolo, M. Degano, and N. Bianchi, "On the analytical estimation of the airgap field in synchronous reluctance machine," in *Proc. Int. Conf. Electr. Mach. (ICEM)*, Sep. 2014, pp. 239–244.

[17] M. Farhadian, M. Moallem, and B. Fahimi, "Analytical calculation of magnetic field components in synchronous reluctance machine accounting for rotor flux barriers using combined conformal mapping and magnetic equivalent circuit methods," *J. Magn. Magn. Mater.*, vol. 505, Jul. 2020, Art. no. 166762.

[18] F. Cupertino, G. Pellegrino, and C. Gerada, "Design of synchronous reluctance motors with multiobjective optimization algorithms," *IEEE Trans. Ind. Appl.*, vol. 50, no. 6, pp. 3617–3627, Nov. 2014.

[19] M. Palmieri, M. Perta, F. Cupertino, and G. Pellegrino, "Effect of the numbers of slots and barriers on the optimal design of synchronous reluctance machines," in *Proc. Int. Conf. Optim. Electr. Electron. Equip. (OPTIM)*, May 2014, pp. 260–267, doi: 10.1109/OPTIM.2014.6850947.

[20] J. Kennedy and R. Eberhart, "Particle swarm optimization," in *Proc. Int. Conf. Neural Netw. (ICNN)*, Nov. 1995, pp. 1942–1948, doi: 10.1109/ICNN.1995.488968.

[21] J. J. Liang, A. K. Qin, P. N. Suganthan, and S. Baskar, "Comprehensive learning particle swarm optimizer for global optimization of multimodal functions," *IEEE Trans. Evol. Comput.*, vol. 10, no. 3, pp. 281–295, Jun. 2006.

[22] Y. Wang, G. Bacco, and N. Bianchi, "Geometry analysis and optimization of PM-assisted reluctance motors," *IEEE Trans. Ind. Appl.*, vol. 53, no. 5, pp. 4338–4347, Sep. 2017, doi: 10.1109/TIA.2017.2702111.

[23] P. Niazi, "Permanent magnet assisted synchronous reluctance motor, design and performance improvement," Ph.D. dissertation, Dept. Elect. Comput. Eng., Texas A&M Univ., Kingsville, TX, USA, 2006.

[24] G. Pellegrino, T. M. Jahns, N. Bianchi, W. L. Soong, and F. Cupertino, *The Rediscovery of Synchronous Reluctance and Ferrite Permanent Magnet Motors: Tutorial Course Notes*, 1st ed. Cham, Switzerland: Springer, May 2016.

MOEIN FARHADIAN received the M.Sc. degree in electrical engineering from the Isfahan University of Technology, Iran, in 2017, where he is currently pursuing the Ph.D. degree. His research interests include electric machine modeling, analysis, and design optimization using advanced analytical and numerical methods with a special interest in synchronous and switched reluctance motors.

MEHDI MOALLEM (Senior Member, IEEE) received the Ph.D. degree in electrical engineering from Purdue University, West Lafayette, Indiana, in 1989. He has been with the Department of Electrical and Computer Engineering, Isfahan University of Technology, Isfahan, Iran, since 1990. He has authored more than 150 peer-reviewed journals and conference papers. His current research interests include the design and optimization of electromagnetic devices, application of advanced analytical and numerical techniques in electric machine modeling, analysis and diagnosis, and power quality.

BABAK FAHIMI (Fellow, IEEE) received the B.S. and M.S. degrees (Hons.) in electrical engineering from the University of Tehran, Iran, in 1991 and 1993, respectively, and the Ph.D. degree in electrical engineering from Texas A&M University, in 1999. He has coauthored over 375 peer-reviewed articles and holds 22 U.S. patents. He has been active in research on electric machines and drives over the past 30 years. He is the advisor for 36 Ph.D. degree students and 30 M.S. degree students.